Directed Assembly of Bimetallic Nanoparticles by Pulsed-Laser-Induced Dewetting: A Unique Time and Length Scale Regime

Jason D. Fowlkes,[†] Yueying Wu,[‡] and Philip D. Rack*[,†,‡]

Center for Nanophase Materials Sciences, Oak Ridge National Laboratory, Oak Ridge, Tennessee 37831, and Materials Science and Engineering Department, University of Tennessee, Knoxville, Tennessee 37996

ABSTRACT Pulsed-laser-induced dewetting (PLiD) was used to assemble patterned, nanoscale metallic thin film features into bimetallic nanoparticles. The liquid-phase flow is related to a conventional droplet impact test and, in appropriate dimensions, have inertial and viscoinertial flow characteristics. The final size, morphology, composition, and interdiffusion of the nanoparticles is governed by the interplay of capillary, inertial, and viscous forces and an appropriate dimensional regime defined by competing Rayleigh-Plateau and spinodal instabilities.

KEYWORDS: dewetting • thin film • self-assembly • capillary force • Plateau-Rayleigh • spinodal • Rayleigh-Plateau • pulsed laser induced dewetting

The synthesis and assembly of functional nanomaterials with unique properties is critical for realizing many of the overarching goals of nanoscience and nanotechnology. The future of nanomaterials synthesis will likely require the confluence of both top-down and bottom up self-assembly techniques. Bottom-up approaches leverage both self-assembly and self-organization via structure formation in thermodynamic systems far from equilibrium (1). Top-down methods make it possible to prescribe the initial state of a system. Thus, by predetermining or "encoding" a system far from equilibrium a desired final state may be achieved by following the assembly process toward a minimization of free energy. Self-assembly at the nanoscale typically involves weak interactions leading to the spatial orientation of building blocks into ordered arrays. Although chemists have exploited weak interactions extensively (2) in the design and synthesis of self-assembled molecules (3), it is important to extend these self-assembly principles to the nano-, micro-, meso-, and even macroscale systems (4).

One important "weak interaction" that has been exploited to assemble materials at multiple length scales is the capillary force (5, 6). Microscale assembly of three-dimensional electrical, optical, and electromechanical elements has been demonstrated using capillary forces by controllably folding planar microfabricated elements into three-dimensional objects. Limited mesoscale examples exist; however, the assembly of three-dimensional, millimeter polyhedral elements with electrical interconnectivity has been demonstrated (7). Thus, although some success has been realized in the self and directed assembly at micro and meso length scales, fundamental questions remain regarding the utility of capillary driven assembly at the nanoscale.

In this article, we describe the use of top down nanoscale lithography and the subsequent directed assembly to synthesize bimetallic nanoparticles driven by capillary forces in the liquid phase. We have successfully synthesized bimetallic Ni−Cu nanoparticles with controllable placement, size, composition, shape, and interdiffusion. Tailored fluid retraction was "encoded" by patterning conjoined thin films, each with a triangular prism shape, to form a Ni−Cu rhombohedron. The triangular faces of the prisms were positioned in the substrate plane where a desired in-plane curvature could be prescribed into the films by changing the vertex angles. The triangular faces were either equilateral or isosceles. The binary prism couple, or rhombohedron, was adjoined in such a way as to share a common triangle base edge. The thin film thickness dimension corresponded with the side length of the prism. For the case of prisms with isosceles faces, we will subsequently refer to the smaller angle of the isosceles face as (α) and the larger angle as (β). In addition, we will refer to triangular prism thin films as simply "prisms" hereafter.

Pulsed laser heating above the melt threshold ultimately initiated the nanoscale assembly. The idea of assembling binary thin films into nanoparticles evolved from our initial characterization of pulsed laser induced dewetted features resulting from patterned nickel shapes (8). The initial thin film shapes were synthesized using standard electron beam lithography and DC sputter deposition on silicon wafer substrates (see the Supporting Information, S1). When the

* Corresponding author. E-mail: prack@utk.edu.
Received for review May 12, 2010 and accepted June 25, 2010
[†] Oak Ridge National Laboratory.
[‡] University of Tennessee.
DOI: 10.1021/am100417x
2010 American Chemical Society

patterned metal films were exposed to a laser fluence exceeding the melt threshold, fluid retraction of the melted nanostructures revealed that the vertex retraction velocity exceeded the edge retraction velocity. This observation suggested that the in-plane curvature affects the fluid transport.

These observations and the challenge of synthesizing advanced multicomponent/multifunctional nanoparticles led us to explore the directed assembly of nanoparticles via the pulsed laser induced dewetting (PLiD) of nanopatterned thin films. As will be demonstrated, by controlling (via lithography) the in-plane dimensions and consequently the vertex angles of the two adjoined thin film prisms, the laser induced melting and subsequent fluid flow could be directed to create bimetallic nanoparticles with controllable composition, size, shape, and interdiffusion. It was also recognized that competing Plateau-Rayleigh (9, 10) and spinodal dewetting (11–13) instabilities (see ref 14 for recent review) could be operative at certain time and length scales. Additionally, opposing viscous and inertial forces compete with capillary forces that govern the directed assembly flow (see ref 15 for recent review). The focus of this study is to (1) describe how the in-plane ($x-y$) and out-of-plane (h, film thickness) length scales lead to the nanoparticle directed assembly; (2) evaluate the relevant capillary, inertial and viscoinertial forces that are involved; and (3) a briefly examine appropriate length and time scales of competing instabilities that ultimately define the unique regime in which we can direct the assembly of bimetallic nanoparticles.

Nanosecond PLiD offers a unique method to probe the dynamics and control the assembly of nanoscale materials because the patterned solid shapes and rapid heating and cooling rates enable us to "freeze" the fluid retraction prior to reaching the equilibrium morphology. The extent that the patterned thin films are out of equilibrium immediately after the solid-to-liquid phase transformation is demonstrated by comparing the energy state of an equivalent spherical liquid nickel droplet (radius =146 nm) to a liquid nickel prism with an equilateral triangular face that is 25 nm thick with an edge length of 1 μm. Assuming mass conservation, the energy difference between the liquid nickel drop and the liquid prism is 7.3×10^{-13} J. Realizing the equivalent kinetic energy requires a hypothetical droplet impact velocity of 123 m/s. Accelerated by gravity, this would require an effective drop height of more than 1.5 km!

Following Bartolo et al. (16), the retraction dynamics of a liquid film created by a drop impact can be correlated to the dynamics of the original droplet impact. Depending on the combination of forces that are operative, dewetting flow can be classified as inertial, viscoinertial, or viscous (17–20). Thus, for our hypothetical nanoscale droplet impact test (and ignoring the obvious subtle differences in the radial symmetry of a circular droplet), the governing forces that are operative in the droplet impact (and subsequent dewetting process) can be estimated by evaluating various dimensionless parameters. For instance, the Reynolds number ($Re = \rho x V/\eta$), the Ohnesorge number ($Oh = \eta/(\rho\chi\gamma)^{1/2}$), and the Weber number ($We = \rho x V^2/\gamma$) relate the relative ratios of the inertial/viscous, viscous/(capillary and inertial), and inertial/capillary forces, respectively, where x, for the drop impact, is the droplet radius, η is the liquid viscosity (4.7×10^{-3} Pa/s), ρ is the liquid density (7800 kg/m^3), γ is the liquid−vapor surface energy (1.78 J/m^2), and V is the impact velocity calculated above. On the basis of these parameters, our hypothetical droplet impact test results in $Re = 30$, $Oh = 0.1$, and $We = 9.7$. These dimensionless parameters collectively suggest that the operative forces during the subsequent retraction of the resultant film (i.e., our patterned and laser melted nanostructures) are initially governed by a competition between capillary and inertial forces. As we will show, by increasing the triangular area of the prism (at constant film thickness), the increased travel distance required to form a single particle leads to a dewetting scenario governed by viscoinertial, and even viscous, forces in concert with the capillary force. In this scenario, the excess volume accumulates at the retracting vertices and edges as a rim indicating an evolving viscous resistance.

To understand the nanostructured film retraction dynamics as well as the limits of the various thin film geometries (i.e., length scales) that form a single droplet, a series of different copper and nickel nano- and microscale thin film structures were synthesized, laser irradiated, and imaged by scanning electron microscopy (SEM). Figure 1a shows a collection of plane view SEM images of one series of 25 nm thick nickel prisms that were synthesized and exposed to a single 420 mJ/cm^2 laser pulse. A simulation of the laser-induced melting process suggests a liquid nickel lifetime of ~26 ns. Each prism has an isosceles triangle face with a common base width (~530 nm) where each row in the figure has a variable triangle face length (l). Each column replicates the pattern array for statistical purposes. Figure 1b shows tilted (60° from vertical) SEM images of a select column illustrating that each prism dewets during a single laser pulse and assembles into a single particle. The measured average contact angle for the images in Figure 1b (~126 ± 6°) is in good agreement with the calculated equilibrium contact angle for liquid nickel supported on a silicon substrate (~110°).

Figure 2a shows several plots derived from experimental data where a variety of patterned nickel prisms, with isosceles triangular faces, converged to single drops. First of all, the ratio of the α vertex-to-nanoparticle center distance to the base vertex-to-nanoparticle center distance (see inset) is plotted versus the vertex angle α (where the base angle, $\beta = (180 - \alpha)/2$). Several interesting observations can be gleaned from Figure 2. As expected, the ratio of the α/β vertex-to-droplet center distances approaches unity for $\alpha = 60°$ (i.e., an equilateral triangle face). The final droplet position consistently coincided with the geometric centroid of the initial triangular face. As a result, for $\alpha < 60°$, the α vertex must travel farther in order to collapse into a single droplet relative to the β vertex of wider angle. Intuitively we expected the fluid flow to follow each angle's bisector, which all intersect at the triangle in-center position. Figure 2a also

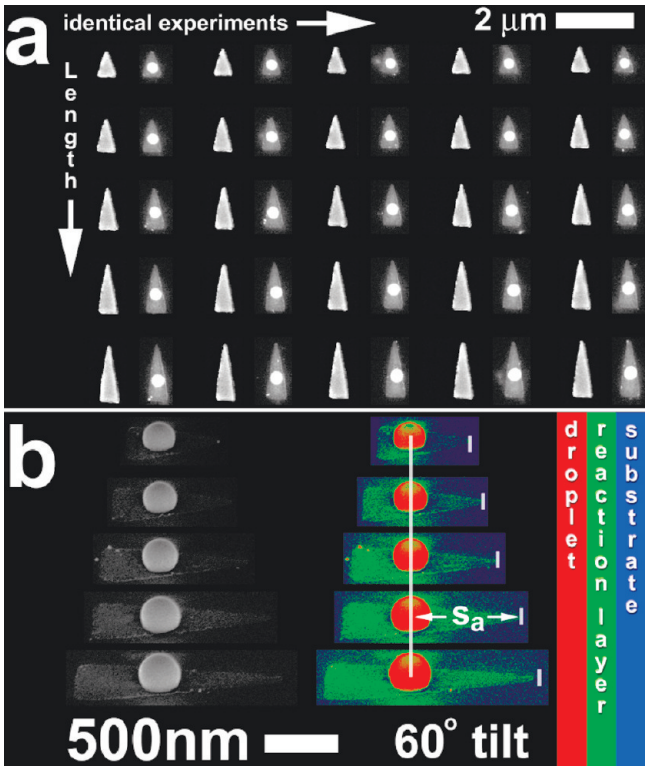

FIGURE 1. (a) SEM images of an array of nickel thin film prisms (with triangular faces in the substrate plane) imaged before and after pulsed-laser-induced dewetting (PLiD). Each prism has a constant triangular base width (530 nm), an edge thickness (25 nm), and each row has a different triangular face length. A thin reaction layer reveals the original triangular face dimension in the dewetted images. (b) Images of dewetted prisms acquired at 60° with respect to the substrate surface normal revealed the spherical shape of the droplet. The falsely colored secondary electron contrast image emphasizes the droplet (red), reaction layer (green), and the substrate surface (blue).

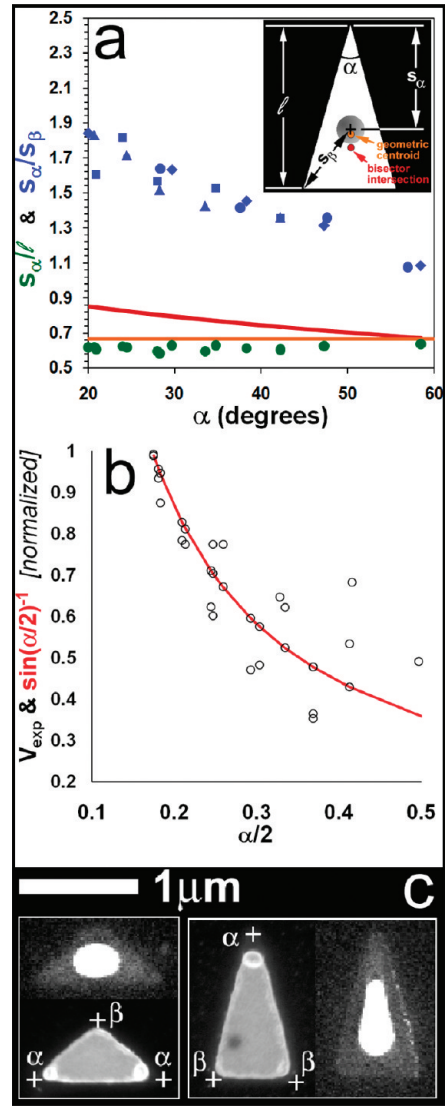

FIGURE 2. (a) Final droplet position (s_α/l) versus vertex angle (α) following pulsed-laser-induced dewetting (green circles), which trends to the geometric centroid (orange line) of the initial, triangular dimension rather than the in-center position (red-line). Blue symbols show the ratio s_α/s_β (see inset for description) versus α, which suggests that the more acute angle travels faster during PLiD. (b) Experimentally observed α vertex retraction velocity as a function of vertex half angle (data points). A modified capillary number Ca × sin(α/2) predicts well the observed increase in the retraction velocity with decreasing vertex half angle α/2. (c) SEM images comparing the equivalent prisms exposed to a low fluence (thus short liquid lifetime, 1−2 ns) and a high fluence (thus a longer liquid lifetime, 26 ns). Note the change in the assignment of the α angle for the left prism because the base angle is the smaller angle.

shows a plot of the final nanoparticle position (normalized to the triangle length) versus the angle α; the data consistently lie at the geometric centroid (2/3 of the triangle length to the α vertex) and do not follow the in-center position. We interpret the final position of the solidified droplet as an indication of a larger retraction velocity for fluid located at α, relative to β, for $\alpha < 60°$. We attribute the increased velocity at more acute angles to a modification of the effective capillary number ($Ca = \eta V/\gamma$) to Ca × sin(α/2), where α/2 is the vertex half angle, which is consistent with the evolution of a "cornered drop" at the receding contact line for the condition of a high inclination angle (and subsequently a higher droplet velocity) (21). The effect of the modified capillary number is an increase in the retraction velocity by $V/\sin(\alpha/2)$. Figure 2b shows a normalized plot of $\sin(\alpha/2)^{-1}$ and the measured vertex velocity versus α, which shows very good agreement between the experimental results and the assumption of a modified capillary number. To confirm this, we synthesized a second set of identical prisms and exposed them to a laser fluence slightly larger than the simulated melt threshold (320 mJ/cm^2), which resulted in a liquid lifetime of just 1−2 ns. Figure 2c compares identical prism thin films that received both brief (1−2 ns) and longer (26 ns) liquid lifetimes. The resulting morphologies demonstrate that the resultant nanoparticle position is consistent with the $V/\sin(\alpha/2)$ dependence of the retraction velocity; after only 1−2 ns, the vertex retraction and subsequent Ni rim accumulation for smaller angles is clearly more significant than the accumulation at the wider (β) angle locations. This result is consistent with an increase in the vertex velocity with decreasing in-plane angle.

On the basis of these observations, we surmised that a rhombohedron-shaped thin film should also converge to the geometric centroid and, the question arose, would the convergence be preserved if the rhombohedron shape

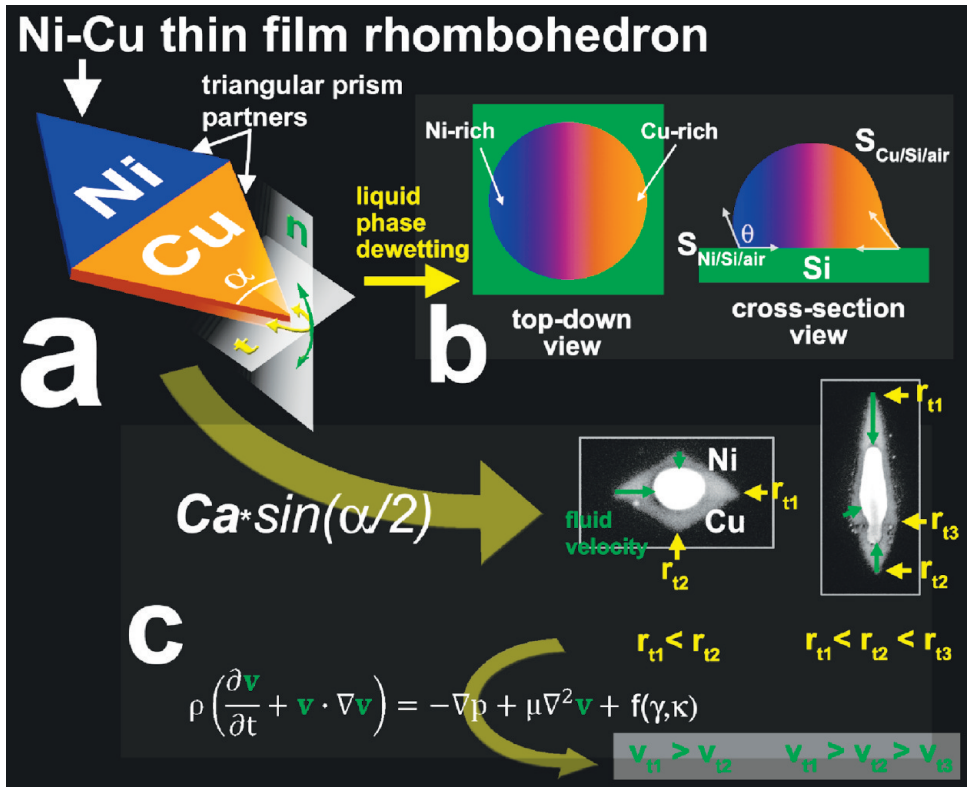

FIGURE 3. Schematic illustration of the pulsed-laser-induced dewetting (PLiD) method. (a) Two iterations of electron beam lithography and metallization are required to produce the rhombohedron structure shown where binary, triangular prism thin films are adjoined at their common triangular base edge. Key to the formation of the single droplet is the continuous boundary at the Ni−Cu interface. Out-of-plane ("n", normal) and in-plane ("t", tangential) curvature act in concert to force the shape change toward a droplet morphology during the liquid phase dewetting process; behavior predicted by a modified capillary number (Ca × sin(α/2)) which is dependent on the vertex angle (α). (b) Steady-state shape following PLiD where S is the spreading parameter and θ is the equilibrium wetting angle. The top-down illustration shows Ni-rich and Cu-rich ends separated by a diffuse region formed by controlled Ni and Cu interdiffusion that occurs during the brief melt time. (c) Smaller vertex angles produce larger retraction velocities as a consequence of the interplay between surface curvature and tension. This term is appended to the Navier−Stokes equation. The small "r" in c refers to the radii of curvature of the indicated indices, γ the liquid−vapor surface tension, κ the local curvature, and V the subsequent retraction velocity.

consisted of two materials delineated by an axis of mirror symmetry? If possible, fluid transport could then be driven to a designed interface in a controlled fashion by directing the liquid phase assembly with top-down lithography. Ultimately we could in practice control the precise location, the final composition, degree of alloying and spatial orientation in the plane dimension for an array of multicomponent/multifunctional nanoparticles. An illustration of a hypothetical, rhombohedral nickel−copper binary pair is shown in Figure 3a. The in-plane (or tangential shown as "t" in Figure 3a) and out-of-plane (or normal shown as "n" in Figure 3a) curvature components drive liquid phase assembly and effectively act in concert to accumulate material at the geometric centroid during PLiD. The initial out-of-plane curvature component is of course governed by the film thickness, and the in-plane curvature is governed by the lithographically defined geometry. The brevity of the laser pulse (25 ns) allows one to control the evolution of the dewetted morphology due to the short liquid lifetime and rapid resolidification; multiple pulses can be used to control the hydrodynamic transport and interdiffusion and thus a variety of metastable shapes and compositions. In addition, Favazza et al. have demonstrated that consecutive "independent" laser-induced melting and resolidification iterations do not disturb the anticipated, final morphological state for nanostructures evolved for instance via spinodal instabilities (22).

The number of laser pulses required to drive the liquid into the final, equilibrium shape depends on the laser fluence and the optical and thermophysical thin film and substrate properties as well as the thin film thickness and area. For the typical dimensions demonstrated here, the formation of particles illustrated in Figure 3b occurred after 1−5 laser pulses (420 mJ/cm^2, 25 ns 248 nm wavelength laser exposure), see the Supporting Information, S2. The top-down illustration shows the anticipated final particle composition where both Ni-rich and Cu-rich quarter spheres are delineated by a region of interdiffusion. Figure 3b also shows an illustration of the cross-section of the micro/nanoparticle where the wetting angle of the nanoparticle is dictated by the balance of the liquid−solid−vapor surface tensions as described by Young's equation ($\gamma_{sl} + \gamma_{lv}\cos\theta = \gamma_{sv}$) where θ is the equilibrium wetting angle.

Figure 3c shows the resulting dewetted pattern of two Ni−Cu thin film rhombohedrons that had different initial, in-plane shapes. One laser pulse was applied to each. The in-plane angle present at each vertex clearly affected the retraction velocity/distance as indicated by the green vectors superimposed over the SEM images. Consistent with Figure 2b, smaller vertex angles induced a larger average retraction

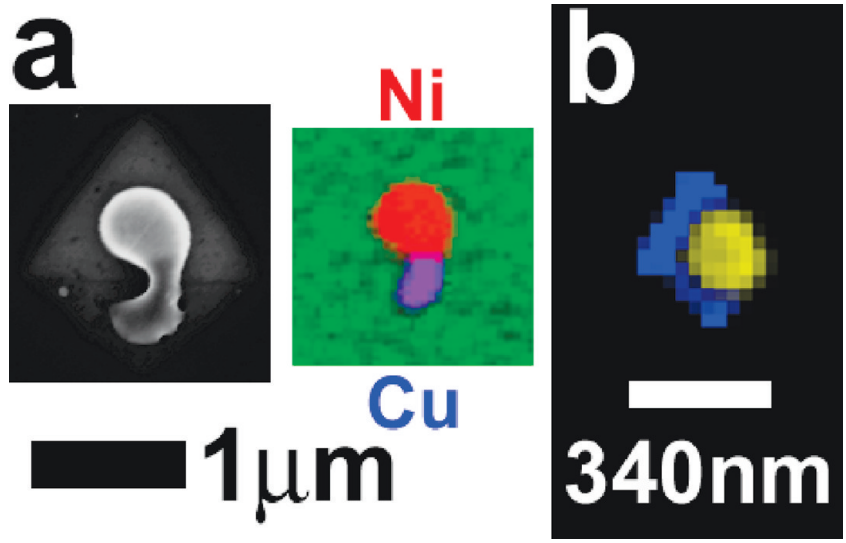

FIGURE 4. (a) Single laser pulse (liquid lifetime, $\tau_m \approx 26$ ns) produces a merged droplet with a distinct material boundary demonstrated by secondary electron contrast; nickel has a relatively larger secondary electron yield than copper. An Auger electron microscopy (AES) map confirmed the contrast revealed in the SEM image for the merged particle shown (the green channel in the image represents silicon. (b) Falsely colored, overlapping SEM image collage of the smallest fused particle (yellow) thus far confirmed by experiment. The initial rhombohedron feature (blue) was overlapped precisely with the resultant dewetted nanoparticle (yellow) using global alignment marks registered on the sample.

velocity. It is important to note that we define the average retraction velocity as $\Delta s/\tau_{melt}$ where Δs is the change in edge/vertex position after the total liquid lifetime τ_{melt}. The simulated τ_{melt} for the 25 nm thick Ni and Cu is 26 ns and 74 ns, respectively. The proportionality between vertex curvature, i.e., angle, and average retraction velocity made it possible to control the final binary particle composition by simply adjusting the ratio of the initial triangular prism face length (l) for the two materials (length in the substrate plane measured for each prism from the common base where the two materials are joined at the axis of symmetry—not to be confused with the thin film thickness). For example, Figure 3c shows an SEM image of an acute Ni prism with a large in-plane triangle face length, with respect to its adjoined Cu prism partner with a smaller triangle face length (i.e., designed to produce a Ni-rich particle) that merged into a single particle. Figure 3c also shows that the binary dewetting process evolves toward the geometric centroid of the rhombohedron formed by the adjoined prisms. An initial combinatorial array of binary nanoparticles was synthesized with varying nanoparticle sizes (total volume of both the 25 nm thick Cu—Ni prisms) and compositions (relative planar areas of the two triangular faces). Figure 4a shows SEM images of a ~60 % Ni/40 % Cu rhombohedron before and after a single laser pulse. A complementary Auger electron map of the Cu (blue) and nickel (red) and silicon substrate (green) is also shown. The smallest binary pair that successfully merged into a single nanoparticle is shown in figure 4b) where we have colorized and merged the original rhombohedron (blue) with the resultant laser treated nanoparticle (yellow). A ~200 nm nanoparticle was observed to form from a rhombohedron designed to yield a composition of Ni-0.3Cu (neglecting possible evaporation and/or diffusion into the substrate) in a single laser pulse. The image also shows the position of the nanoparticle in relation to the original metal pattern prior to dewetting.

The spatial orientation of the composition gradient, determined by the original prism alignment, is preserved following the dewetting process. Auger electron spectroscopy (see the Supporting Information, S3) was used to generate a qualitative composition map of dewetted particles following a single laser pulse and the results are displayed in Figure 5. The figure was arranged to demonstrate the spatial composition per particle as a function of the intended composition. In addition, four particles are shown for each composition to demonstrate reproducibility. It is important to note that the total, average particle composition is dictated by the ratio of triangular face area for each prism (for constant rhombohedron thickness) but that the distribution/intermixing of each particle is dictated by the time—temperature profile of the laser pulse(s), which drives the interdiffusion and hydrodynamics of the binary species. Figure 4a demonstrates that the particle composition is far from spatially homogenized; these particles contain composition gradients where Ni- and Cu-rich ends were separated by a transition region where Ni—Cu interdiffusion occurred, albeit briefly.

To understand the various instability mechanisms that can affect the final dewetted morphology, we synthesized 3 specific thin film prism geometries: (1) prisms with highly isosceles triangle faces (constant film thickness); (2) prisms with larger triangle faces with constant film thickness; and (3) decreased prism thickness. Each of these geometries illustrates a different dimensional constraint for the PLiD directed assembly process. Figure 6 demonstrates 3 nickel prisms ($h = 25$ nm) that were pulsed-laser-treated and that have a common triangle face base width of 260 nm but with changing lengths of 600, 1210, and 1860 nm. As can be seen, at a critical length the prisms ultimately fragment into

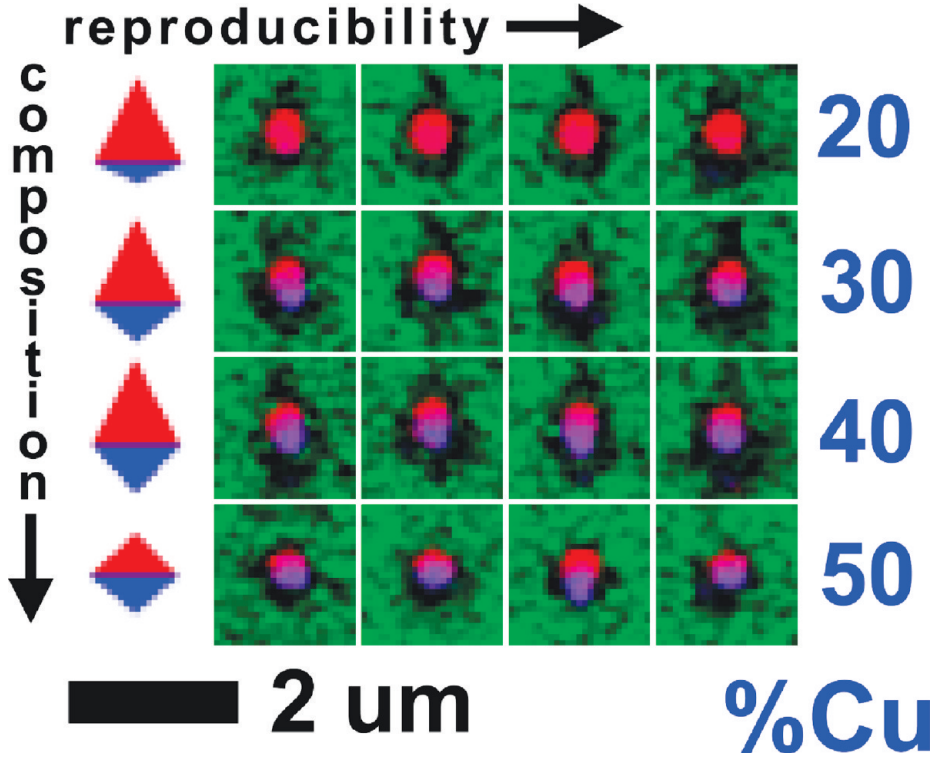

FIGURE 5. Auger electron spectroscopy (AES) composition maps of select particles after a single dewetting pulse. Each row represents a select composition. The maps are qualitative as shown without regard to atomic sensitivity factors. Composition is defined in the red−green−blue coordinates as Ni, Si, and Cu, respectively. The maps reveal Ni- and Cu-rich particle quarter spheres reflecting the composition profile. The unidentified region (black) surrounding each dewetted particle is suspected to be a layer of silicide, perhaps Ni_xSi_y and/or Cu_xSi_y, formed by the reaction of a nanoscale precursor film, material left behind during droplet retraction, with the substrate surface. The nature of this layer has not been fully quantified.

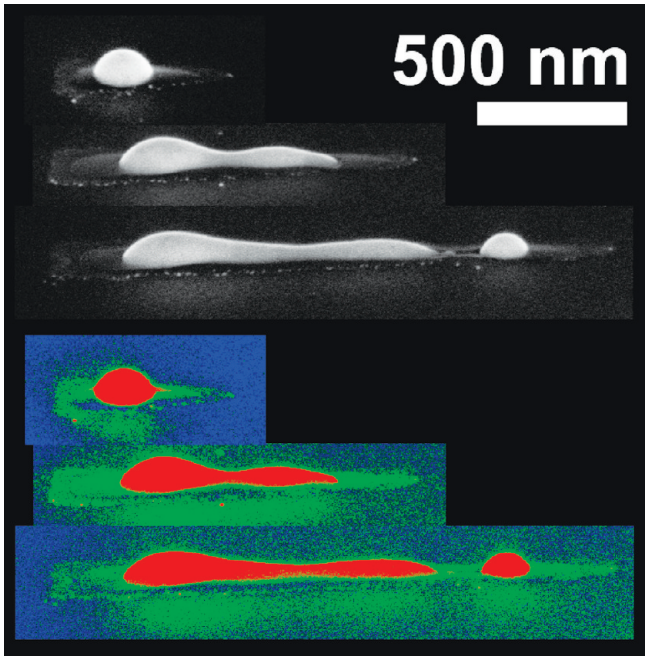

FIGURE 6. SEM images (60° tilt) of resolidified droplets following a single laser pulse. A series of prisms are shown that have a common base width of 260 nm and various lengths of 600, 1210, and 1860 nm. Resolidified prisms with large aspect ratios (l/*w*) exhibit the formation of a Plateau-Rayleigh instability leading to the formation of multiple particles/rivulets.

multiple particles. The dispersion observed in the particle spacing is characteristic of the propagation of the Plateau-Rayleigh instability observed in cylindrical liquid jets. We attribute the Plateau-Rayleigh characteristic, for the cases of $l = 1210$ and 1860 nm, to the convergence of the narrow α vertex prism geometry, to a rivulet geometry, as $\alpha \rightarrow 0$ (9, 10). Ignoring substrate effects (24, 25), the upper limit for l can be estimated from the Plateau-Rayleigh instability criteria where surface perturbations of wavelength $\lambda > 2\pi r$ are stable and propagate in amplitude. The maximum velocity occurs for a perturbation of $\lambda = 9.02r$, where r is the rivulet radius. If one assumes a highly isosceles triangular face, such that the prism geometry approaches that of a rivulet, then the equivalent rivulet radius is $r = (bh/\pi)^{1/2}$, where b is the triangular base width and h is the film thickness. This ideal picture is complicated by the fact that the prisms retract as the Plateau-Rayleigh instability evolves. If one accounts for this contraction, estimated using the Taylor-Culick (26, 27) inertial flow velocity $V = (|S|/\rho h)^{1/2} = 111$ m/s and based on the equilibrium spreading parameter ($S = -2.41$ N/m), the estimated critical length of the triangular prism face (with a 260 nm base width) was calculated to be 1035 nm. This value is in good agreement with the prism ($l = 1210$ nm) that demonstratively showed a propagating instability following resolidification (Figure 6).

Fluid retraction governed by viscoinertial forces was explored by increasing the area of the triangular prism face length and base. Figure 7 shows an example set of prisms that have the common dimensions of $\alpha \approx 42°$ and $\beta \approx 69°$, $h = 25$ nm, $b = 4.17$ μm, and $l = 5.42$ μm (the bottom figure shows a higher resolution, 60° tilted view of

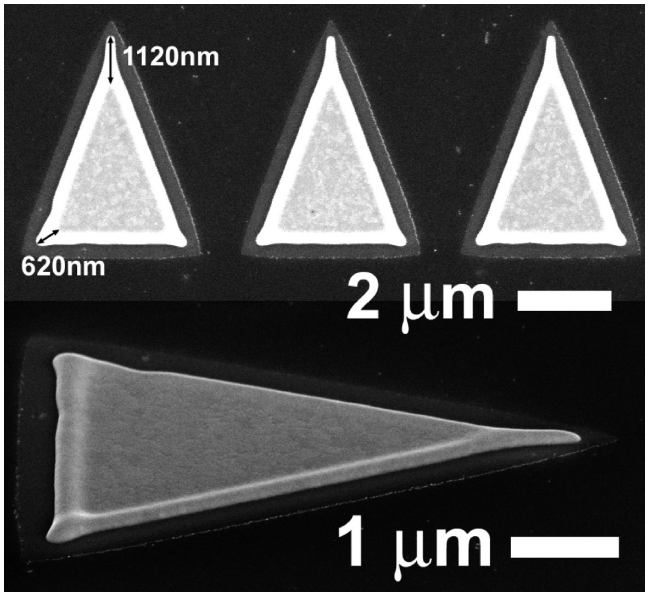

FIGURE 7. SEM plane-view (top) and 60° degree tilted (bottom) images of larger prisms (compared with the prisms shown in Figure 1a) demonstrating rim formation, accumulated during fluid retraction, which changes the effective flow regime from inertial/capillary to viscoinertial/capillary.

the leftmost prism imaged in plane-view). Here, the total distance traveled (and the resulting average velocity) for the α and β vertices as well as the edge dimension were 370 nm (14.2 m/s), 440 nm (16.9 m/s), and 340 nm (13.1 m/s), respectively. An estimate of the distance an edge will travel (Δs) before transitioning from inertial to viscoinertial flow is given by $\Delta s = |S|^{1/2}h^{3/2}\rho^{1/2}/\eta$ (19) and suggests a liquid nickel edge travel distance of ~145 nm. This is equivalent to an effective Ohnesorge number of 1.0 for the accumulating rim. Thus, the traveling rim likely transitioned into the viscoinertial regime during retraction considering that the rim translation exceeded the estimate for Δs. It is interesting to note that the magnitudes of the average velocities of the α and β vertices are opposite to the trends of the smaller prisms (e.g., those shown previously in Figure 1a), which coalesced into single nanoparticles. The vertex angle significantly affects the rim length for the triangular faces of larger area because the rim evolves from the intersection of the two edges that constitute the angle. As demonstrated in Figure 7, the rim that formed at the α vertex position is much longer (1120 nm) than the rim located at the β vertex (620 nm). As a result, the Ohnesorge number of the rim formed at the acute vertex ($Oh(\alpha) = 9.7$) increases faster than Oh at the vertex of wider angle ($Oh(\beta) = 5.7$). The large value of *Oh* indicates that viscous dissipation acts to decelerate material located at the acute vertex. This is analogous to the inverse experiment of a traveling droplet where the receding contact line forms a triangular shape, and at higher velocity, forms a rivulet and eventually daughter droplets (see ref 25 and references therein). Indeed, subsequent laser pulses can induce rim instabilities (28) leading to fingering and/or droplet formation around the rim perimeter.

Finally, the last dewetting mechanism that competes with the nanoparticle directed assembly is the spinodal dewetting mechanism favored for a geometry consisting of a semi-infinite, ultrathin (<10 nm) film. Kalyanaraman et al. have

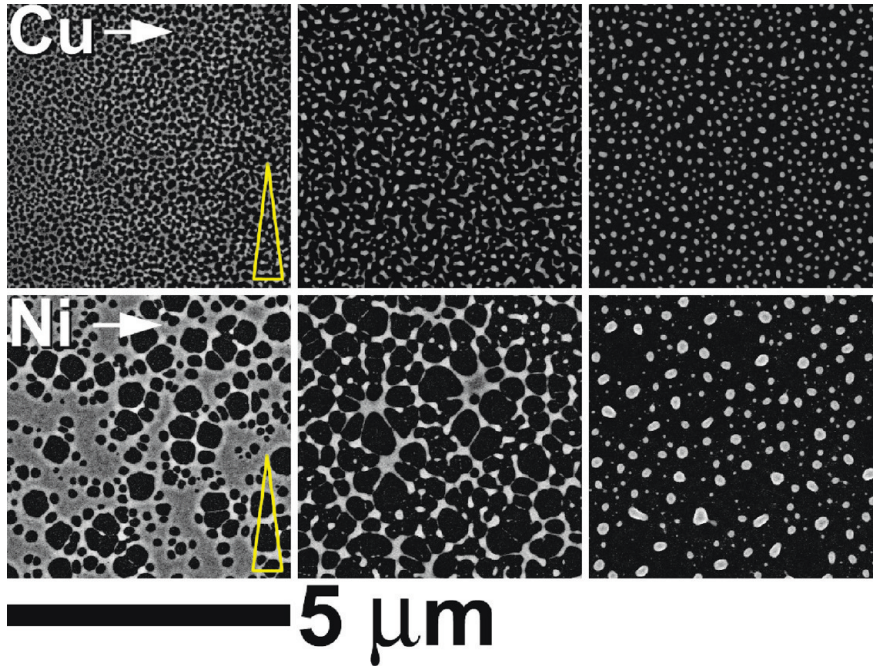

FIGURE 8. Spinodal dewetting evolution in ~6 nm thick copper and nickel thin films. The images were collected at the edge of intersection between the focused laser pulse and the thin films where a steep gradient in laser fluence produces a complementary gradient in liquid lifetime. Thus, SEM image acquisition, starting at the edge of the laser irradiated region and proceeding inward (direction indicated by the superimposed arrow), provides an approximation of the time evolution of the spinodal dewetting process. The superimposed yellow triangles represent prism dimensions that yielded a single particle, in response to PLiD, when the initial film thickness was 25 nm. Conversely, at the reduced film thickness of 6 nm, the superimposed triangle suggests multiple discrete particles would be produced at this triangular face length scale.

recently published a series of papers investigating spinodal dewetting phenomenon in pulse laser treated thin films (22, 29–32). Figure 8 shows a series of SEM images acquired very near the edge of a laser spot used to irradiate ~6 nm thick Cu and Ni films. A significant laser fluence gradient exists at this location which ultimately translates into a complementary gradient in the liquid lifetime (33). By acquiring images along the liquid lifetime gradient we obtained an approximation of the time evolution of the spinodal dewetting morphology. Thus, although the specific cumulative liquid lifetimes are not precisely known, the images demonstrate the temporal evolution of spinodal dewetting for the thin Cu and Ni films on silicon. Hydrodynamic theory reveals the resultant time (τ_s) and length scale (λ_{max}) associated with the fastest growing surface perturbation is given by: $\lambda_{max}(h) = (16\pi^3\gamma)/A)^{1/2}h^2$, and $\tau_s(h) = (96\pi^2\eta\gamma)/(A^2)h^5$, where A is the Hamaker coefficient. Because of the magnitude of the Hamaker coefficient is ~1 $\times 10^{-18}$ to 1 $\times 10^{-20}$ J, this mechanism is operative only at nanometer to tens-of-nanometers film thickness. Thus, to assemble very small triangles with very thin films, the directed transport must compete with the time and length scale associated with the spinodal dewetting process. Considering the various prism geometries previously shown in Figures 1a, 6, and 7, the images presented in Figure 8 clearly indicate that the spinodal dewetting process will disrupt prescribed single nanoparticle formation for ultrathin films (<10 nm) unless the lateral dimension of the prisms are made smaller than the spinodal wavelength (i.e., the average hole spacing in the leftmost images shown in Figure 8) or the effective retraction time must be less than the spinodal dewetting time scale. For example, the superimposed yellow triangles shown in Figure 8 represent prism dimensions that yielded a single particle, in response to PLiD, when the initial film thickness was 25 nm. Conversely, at the reduced film thickness of 6 nm, the figure illustrates that multiple individual particles would be produced within the confines of the superimposed prism geometry (ignoring edge effects).

CONCLUSIONS

The union of top-down synthesis and bottom-up, self-directed assembly will ultimately play a central role in the creation of future functional nanostructures and nanodevices. Here we have demonstrated the confluence of conventional top-down, lithography processes with the bottom-up, PLiD assembly process that converts planar, adjoining binary lithographically defined materials into three-dimensional bimetallic nanoparticles with spatially oriented composition gradients. The purpose of this paper was to demonstrate the feasibility of using PLiD to convert nonequilibrium, binary material thin film geometries into single particles with controllable placement, size, composition, and intermixing. The assembly process is driven by competing capillary, inertial, and viscous forces during the nanoscale liquid lifetimes. A unique geometry (i.e., length scale) and time scale exists for this directed assembly process where competing Plateau-Rayleigh and spinodal instabilities can compromise nanoparticle formation outside the unique space and time domain. In addition, for relatively large lateral dimensions the accumulation of rim material coupled with the cumulative viscous and inertial forces can ultimately disrupt the condition of constant velocity retraction, leading to edge/vertex deceleration or even the termination of liquid phase retraction. The PLiD method holds promise for the synthesis of multicomponent/multifunctional nanoparticle ensembles. In principle, the process should be scalable to ternary and quaternary materials systems in order to produce trigonal and tetragonal hosohedrons, which will be explored in the future.

Supporting Information Available: Experimental methods and characterization (PDF). This material is available free of charge via the Internet at http://pubs.acs.org.

Acknowledgment. The authors acknowledge support from the Material Sciences and Engineering Division Program of the DOE Office of Science (ERKCM38) for sponsoring the aspects of this work related to understanding the fundamental mechanisms operative during liquid-phase thin film dewetting. P.R. and J.F. also acknowledge that the lithography and electron imaging results reported in this article were conducted at the Center for Nanophase Materials Sciences, Oak Ridge National Laboratory, and sponsored by the Scientific User Facilities Division (SUFD), Office of Basic Energy Sciences (BES), U.S. Department of Energy.

REFERENCES AND NOTES

(1) Prigogine, I.; Lefever, R. *J. Chem. Phys.* **1968**, *48*, 1695–1700.
(2) Whitesides, G. M.; Mathias, J. P.; Seto, C. T. *Science* **1991**, *254*, 1312–1319.
(3) Ariga, K.; Hill, J. P.; Lee, M. V.; Vinu, A.; Charvet, R.; Acharya, S. *Sci. Technol. Adv. Mater.* **2008**, *9*, 014109.
(4) Whitesides, G. M.; Boncheva, M. *Proc. Natl. Acad. Sci. U.S.A.* **2002**, *99*, 4769–4774.
(5) Glotzer, S. C.; Solomon, M. J.; Kotov, N. A. *AIChE J.* **2004**, *50*, 2978–2985.
(6) Hynninen, A. P.; Thijssen, J. H. J.; Vermolen, E. C. M.; Dijkstra, M.; Van Blaaderen, A. *Nat. Mater.* **2007**, *6*, 202–205.
(7) Boncheva, M.; Gracias, D. H.; Jacobs, H. O.; Whitesides, G. M. *Proc. Natl. Acad. Sci. U.S.A.* **2002**, *99*, 4937–4940.
(8) Rack, P. D.; Guan, Y. F.; Fowlkes, J. D.; Melechko, A. V.; Simpson, M. L. *Appl. Phys. Lett.* **2008**, *92*, 223108.
(9) Kondic, L.; Diez, J.; Rack, P. D.; Guan, Y.; Fowlkes, J. D. *Phys. Rev. E* **2009**, *79*, 026302.
(10) Diez, J.; Kondic, L. *Phys. Fluids* **2007**, *19*, 072107.
(11) Becker, J.; Grun, G.; Seemann, R.; Mantz, H.; Jacobs, K.; Mecke, K. R.; Blossey, R. *Nat. Mater.* **2003**, *2*, 59–63.
(12) Bischof, J.; Scherer, D.; Herminghous, S.; Leiderer, P. *Phys. Rev. Lett.* **1996**, *77*, 1536–1539.
(13) Herminghous, S.; Jacobs, K.; Mecke, K.; Bischof, J.; Fery, A.; Ibn-Elhaj, M.; Schlagowski, S. *Science* **1998**, *282*, 916–919.
(14) Craster, R. V.; Matar, O. K. *Rev. Mod. Phys.* **2009**, *81*, 1131–1197.
(15) Bonn, D.; Eggers, J.; Indekeu, J.; Meunier, J.; Rolley, E. *Rev. Mod. Phys.* **2009**, *81*, 739–805.
(16) Bartolo, D.; Josserand, C.; Bonn, D. *J. Fluid Mech.* **2005**, *545*, 329–338.
(17) Jacobs, K.; Seemann, R.; Schatz, G.; Herminghaus, S. *Langmuir* **1998**, *14*, 4961–4963.
(18) Redon, C.; Brochard-Wyart, F.; Rondelez, F. *Phys. Rev. Lett.* **1991**, *66*, 715–718.
(19) Callegari, G.; Calvo, A.; Hulin, J. P. *Colloid Surf., A* **2002**, *206*, 167–177.
(20) Andrieu, C.; Sykes, C.; Brochard, F. *J. Adhes.* **1996**, *58*, 15–24.
(21) Limat, L.; Stone, H. A. *Europhys. Lett.* **2004**, 365–371.

(22) Favazza, C.; Kalyanaraman, R.; Sureshkumar, R. *J. Appl. Phys.* **2007**, *102*, 104308.
(23) Cheng, H.; Lu, Y. J.; Chen, M. *J. Chem. Phys.* **2009**, *131*, 044502.
(24) McCallum, M. S.; Voorhees, P. W.; Miksis, M. J.; Davis, S. H.; Wong, H. *J. Appl. Phys.* **1996**, *79*, 7604–7611.
(25) Snoeijer, J. H.; Grand-Piteira, N. Le; Limat, L.; Stone, H. A.; Eggers, J. *Phys. Fluids* **2007**, *19*, 042104.
(26) Culick, F. E. C. *J. Appl. Phys.* **1960**, *31*, 1128–1129.
(27) Taylor, G. I. *Proc. R. Soc. London, Ser. A* **1959**, *253*, 313–321.
(28) Brochard-Wyart, F.; Redon, C. *Langmuir* **1992**, *8*, 2324–2329.
(29) Trice, J.; Favazza, C.; Thomas, D.; Garcia, H.; Kalyanaraman, R.; Sureshkumar, R. *Phys. Rev. Lett.* **2008**, *101*, 017802.
(30) Trice, J.; Thomas, D.; Favazza, C.; Sureshkumar, R.; Kalyanaraman, R. *Phys. Rev. B* **2007**, *75*, 235439.
(31) Favazza, C.; Kalyanaraman, R.; Sureshkumar, R. *Nanotechnology* **2007**, *19*, 072107.
(32) Krishna, H.; Shirato, N.; Favazza, C.; Kalyanaraman, R. *Phys. Chem. Chem. Phys.* **2009**, *11*, 8136–8143.
(33) Habenicht, A.; Olapinski, M.; Burmeister, F.; Leiderer, P.; Boneberg, J. *Science* **2005**, *309*, 2043–2045.

AM100417X